Environmental Science & Technology

pubs.acs.org/est

Article

Oxidative Dissolution of Arsenic-Bearing Sulfide Minerals in Groundwater: Impact of Hydrochemical and Hydrodynamic Conditions on Arsenic Release and Surface Evolution

Lucien Stolze, Maria Battistel, and Massimo Rolle*

Cite This: https://doi.org/10.1021/acs.est.2c00309

Read Online

ACCESS | Metrics & More | Article Recommendations | Supporting Information

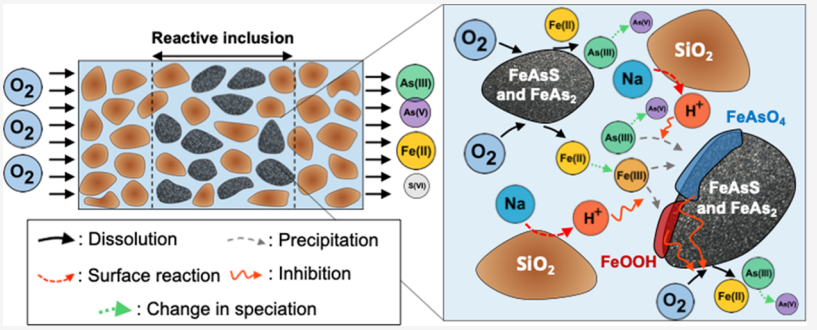

ABSTRACT: The dissolution of sulfide minerals can lead to hazardous arsenic levels in groundwater. This study investigates the oxidative dissolution of natural As-bearing sulfide minerals and the related release of arsenic under flow-through conditions. Column experiments were performed using reactive As-bearing sulfide minerals (arsenopyrite and löllingite) embedded in a sandy matrix and injecting oxic solutions into the initially anoxic porous media to trigger the mineral dissolution. Noninvasive oxygen measurements, analyses of ionic species at the outlet, and scanning electron microscopy allowed tracking the propagation of the oxidative dissolution fronts, the mineral dissolution progress, and the change in mineral surface composition. Process-based reactive transport simulations were performed to quantitatively interpret the geochemical processes. The experimental and modeling outcomes show that pore-water acidity exerts a key control on the dissolution of sulfide minerals and arsenic release since it determines the precipitation of secondary mineral phases causing the sequestration of arsenic and the passivation of the reactive mineral surfaces. The impact of surface passivation strongly depends on the flow velocity and on the spatial distribution of the reactive minerals. These results highlight the fundamental interplay of reactive mineral distribution and hydrochemical and hydrodynamic conditions on the mobilization of arsenic from sulfide minerals in flow-through systems.

KEYWORDS: *sulfide mineral dissolution, arsenic mobilization, surface passivation, flow-through experiments, reactive transport modeling*

INTRODUCTION

Arsenic (As) contamination of groundwater is a global problem threatening the quality of fresh drinking water and the health of millions of people.[1−6] In many aquifers, hazardous levels of arsenic are caused by the dissolution of As-bearing sulfide minerals triggered by dynamic redox conditions where atmospheric oxygen and/or oxic water contact the reduced reactive minerals.[7−12]

Although the dissolution of As-bearing sulfide minerals occurs naturally in the subsurface, anthropogenic activities can exacerbate this contamination by enhancing the exposure of sulfide minerals to oxygen. For instance, the disposal of mine tailings and their exposure to atmospheric oxygen is known to potentially result in the generation of acid mine drainage, triggering the dissolution of a variety of mineral phases and the mobilization of contaminants.[13−17] Managed aquifer recharge (MAR) can also enhance arsenic release in groundwater from the dissolution of sulfide minerals naturally present in the subsurface due to the direct injection of oxic water in the subsurface.[18−22] Furthermore, seasonal fluctuation in water level[23] and hydraulic fracturing[24] have been shown to increase the exposure of sulfide minerals to atmospheric O_2 and, consequently, to enhance their dissolution. Thus, detailed understanding of the geochemical and hydrological processes controlling the dissolution of these As-bearing minerals is fundamental for the adequate understanding of natural and

Received: January 17, 2022
Revised: March 18, 2022
Accepted: March 18, 2022

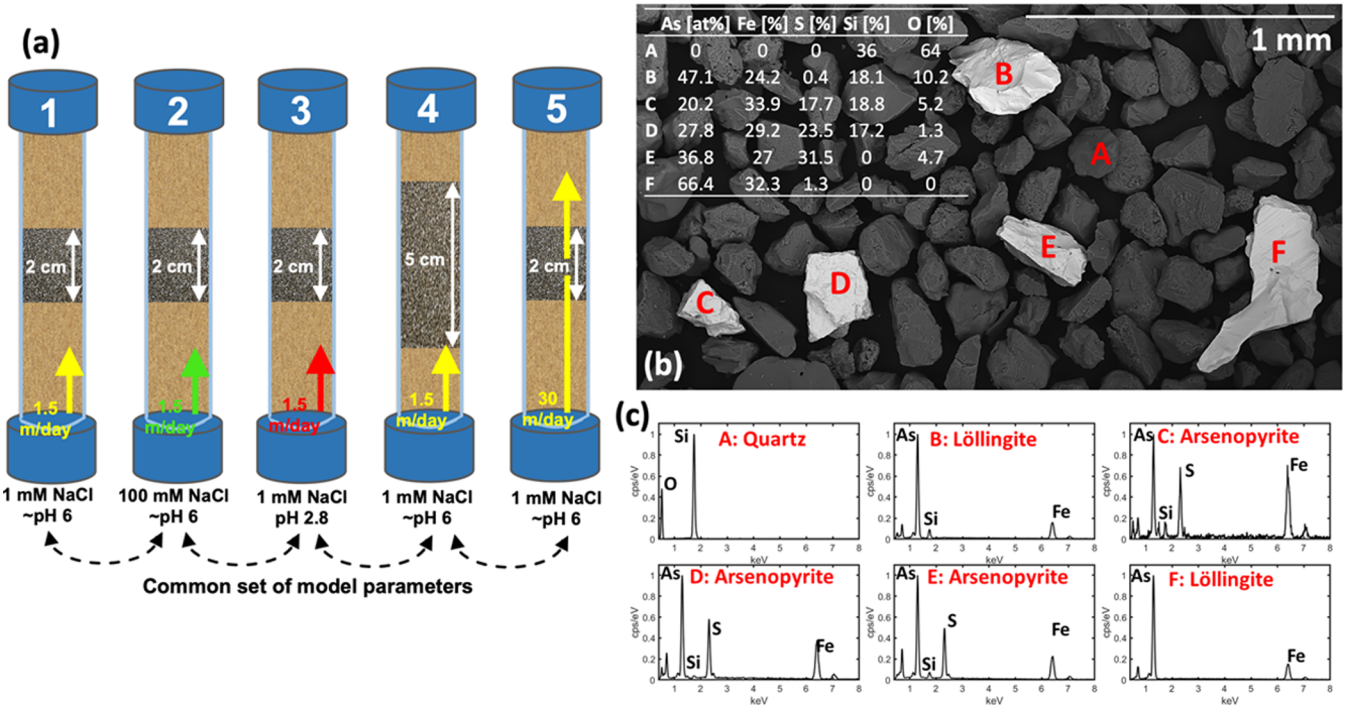

Figure 1. (a) Diagram illustrating the columns with the reactive mineral inclusions, the different hydrochemical and hydrodynamic conditions of the experiments, and the simultaneous calibration approach adopted in the process-based simulations; (b) backscattered electron image of the inclusion and relative elemental composition of selected mineral grains from SEM−EDS measurements shown in atomic percent; (c) spectra of the SEM−EDS measurements performed on the selected mineral grains; and minerals were identified based on the elemental composition.

engineering systems and for improved management of groundwater resources.

Extensive research has been devoted to the characterization of the mechanisms and rates of As-bearing sulfide mineral oxidation and to the subsequent release of arsenic in solution.[25] In particular, multiple oxidative dissolution pathways of sulfide minerals have been identified via the reduction of oxygen, ferric iron, and/or nitrate.[26−30] Furthermore, secondary mineral phase precipitation [i.e., ferric arsenate and/or iron (hydr)oxides] significantly influence the mobility of released aqueous species[7,31] and the rates of the sulfide mineral oxidation via the formation of coatings leading to surface passivation.[32,33] The release and transport of arsenic are particularly affected by the pH and ionic strength as these hydrochemical parameters exert a primary control on a wide range of geochemical processes including sorption and mineral dissolution/precipitation (e.g., refs 34−36). In particular, acidic conditions promote the adsorption of arsenic[37] but increase the solubility of iron oxides. The dissolution of iron oxides is strongly enhanced below pH 4 and reduces the total As sequestration potential of the mineral assemblage.[32,38,39] However, most experimental investigations focusing on As-bearing sulfide minerals have been limited to batch and stirred-flow reactors with single mineral phases and relatively simple hydrochemical conditions. In contrast, a higher level of complexity is expected under natural conditions as a result of (i) the large number of spatially and temporally varying geochemical and physical factors that can affect mineral transformation,[7,40,41] (ii) the heterogeneous spatial distribution of reactive minerals[41−44] and (iii) the coexistence of multiple sulfide minerals with varying kinetic dissolution rates.[29] The complex interplay between multiple co-occurring geochemical and hydrological processes limits our ability to interpret and predict the dissolution of As-sulfide minerals and the release of arsenic in natural systems. Therefore, flow-through laboratory experiments and reactive transport modeling[45−47] are instrumental to provide a quantitative interpretation of the processes controlling the release and transport of arsenic in groundwater.

In this study, we investigate the dissolution of a natural As-bearing sulfide mineral assemblage composed of löllingite and arsenopyrite and the co-occurring release of arsenic during the dynamic change from anoxic to oxic conditions under well-controlled laboratory flow-through conditions. A series of column experiments were performed with the sulfide minerals embedded as inclusions in a sandy matrix with different spatial configuration, forming chemically heterogeneous but physically homogeneous porous media. In particular, we tested the impact of the hydrochemistry (i.e., pH and major ions) on the dissolution of the sulfide minerals and the release of arsenic. Oxic salt and/or acid solutions were injected to trigger the dissolution of the well-characterized As-bearing sulfide minerals under different flow-through conditions. Specific focus was dedicated to the alteration of the sulfide minerals surfaces by microscopy surface characterization techniques. A reactive transport model was developed to provide a quantitative interpretation of the experiments and to analyze the role of co-occurring geochemical and transport processes on the mineral transformation and arsenic mobility.

MATERIAL AND METHODS

Column Experiments. Flow-through experiments were performed in cylindrical glass columns (length: 11.7 cm, inner diameter: 1.75 cm) schematically illustrated in Figure 1. The columns were filled with a wet-packing procedure to minimize the entrapment of air in the pores.[48] The resulting porous

https://doi.org/10.1021/acs.est.2c00309
Environ. Sci. Technol. XXXX, XXX, XXX−XXX

matrix was physically homogeneous, as the quartz sand and the As-bearing sulfide minerals had the same grain size (125−250 μm), but chemically heterogeneous, as the sulfide minerals were embedded as inclusions (10 vol %) in the sandy matrix. The reactive inclusions consisted of 45 wt % arsenopyrite (FeAsS) and 55 wt % löllingite ($FeAs_2$), as shown by scanning electron microscopy (SEM) and energy-dispersive X-ray spectroscopy (EDS) analyses (Figure 1b) and quantified by X-ray diffraction (XRD) analysis.

The experiments were performed by applying a continuous vertical injection from the bottom to the top using two ports at each end of the columns. Steady-state flow conditions with different flow velocities (i.e., 1.5 m/day for experiments 1−4 and 30 m/day for experiment 5) were established by connecting the inlet and outlet ports to high-precision multichannel peristaltic pumps (IPC-N24 and IPC-24, ColeParmer). The column experiments started by flushing the domain with an oxygen-depleted solution (1 mM NaCl and O_2 < 0.022 mM) in order to maintain the setup under anoxic conditions and to equilibrate the surface of the porous media with the initial aqueous conditions. The exposure of the sulfide minerals to O_2 prior to the experiment was minimized by using the sulfide minerals immediately after their preparation (details on the preparation method are provided in the Supporting Information) and by flushing with the oxygen depleted solution at a high flow rate (∼10 m/day) to minimize the time for equilibration. At the beginning of the experiments, oxic solutions with different pH and background electrolyte concentrations (Figure 1) were injected in the column setups.

All columns were equipped with oxygen-sensitive strips (SP-PSt3-NAU, PreSens GmbH, accuracy ± 0.4%) glued onto the inner walls of the setups to track the propagation of the oxygen fronts during the flow-through experiments. We measured high-resolution spatial profiles of O_2 concentrations (5 mm spacing) along the columns at different times. Breakthrough curves of oxygen were recorded before and after the inclusions (i.e., 2 and 9.6 cm from the inlet, respectively) by continuously measuring the oxygen concentration at a 5 min interval. Furthermore, the pH breakthrough curves were monitored at the outlet of the columns by connecting one of the outlet ports to a 10 mL flow-through vial, where a pH electrode (Hach IntelliCAL PHC281) measured pH at a time interval of 5 min. The remaining outlet port was used to measure the eluted solute concentrations during the experiments, with a sampling interval of 1 h. Total Fe and As concentrations and total Na, Al, and S were measured from 2% HNO_3^- acidified samples with inductively coupled plasma mass spectrometry (7700× ICP−MS, Agilent Technologies) and ICP optical emission spectroscopy (ICP-OES, PerkinElmer Avio 200, in axial and/or radial mode), respectively. The confidence in the measurements was ensured by using triplicates and obtaining a measurement standard deviation < 5%. In column experiments 1, 2, and 3, a part of the sample was passed through an arsenic speciation cartridge containing 0.8 g of aluminosilicate adsorbent in order to selectively adsorb As(V), whereas As(III) remained in solution for the analysis.[49,50] The applied flow rates were gravimetrically measured at the end of the column experiments, and the effluent pH breakthrough curves were determined by accounting for dilution effects in the flow-through vial (see the Supporting Information for details). All experiments were conducted at 20 °C and the laboratory solutions were prepared using Milli-Q water.

The effects of pH and ionic strength on the dissolution of As-bearing sulfide mineral and arsenic sequestration during the formation of secondary mineral phases were investigated by performing column experiments with the injection of oxic solutions with different pH values (i.e., pH ≈ 6 and pH ≈ 2.8, the latter obtained by adding 1.6 mM HCl) and with different ionic strengths (i.e., 1 and 100 mM using NaCl as a background electrolyte). These three experiments, denoted columns 1−3 throughout the text, had a 2 cm long inclusion of As-bearing sulfide minerals embedded in the sandy matrix (Figure 1) and were run at flow velocity of 1.5 m/day.

The individual effects of spatial and temporal scales on the mineral transformation and the release of arsenic were assessed by repeating column 1 with a longer mineral inclusion (5 cm, column 4) and with a higher flow velocity (30 m/day, column 5). In particular, such high velocity can represent fast flow observed in highly permeable aquifers and/or during engineering applications where active pumping is applied.[51−54] Details about the preparation and characterization of the porous media and the flow-through experiments are provided in Section S1 of the Supporting Information.

Scanning Electron Microscopy. At the end of the column experiments performed under neutral and acidic conditions (i.e., columns 1 and 3), solid samples from the inclusions were collected for SEM in order to characterize the alteration of the As-bearing sulfide minerals surfaces and to explore the effects of pH on their surface morphology and composition. A sample representative of the inclusion at the beginning of the experiments was obtained by preparing a column (i.e., wet-packing and equilibration with an anoxic solution) that was sacrificed before the injection of the oxic solution. SEM analyses on carbon-coated samples were performed with a Quanta FEG 250 operated at 20 keV and consisted in inspecting the surface morphology and composition with secondary and back-scattered electrons, respectively. Furthermore, surface elemental composition (expressed as atomic percentage [at %]) was analyzed by EDS with an X-Max silicon drift detector (Oxford Instruments). As shown in Figure 1, the SEM analyses performed on the unaltered sample confirmed the outcomes of the XRD analysis showing that both arsenopyrite and löllingite compose the reactive sulfide mineral inclusion and that these minerals are well-segregated in different grains. The higher mass density of the sulfide minerals (bright gray) allows distinguishing them easily from the silica sand grains (dark gray) on the backscattered electron image.

Modeling Approach. The model simulates the transport of oxygen and aqueous charged species introduced in the initially anoxic setups, the interaction between the reactive mineral surfaces and the aqueous charged species, the oxidative dissolution of the sulfide minerals, and the subsequent mineral transformation and leaching of solutes from the reactive minerals. The reactive transport model was implemented in the geochemical code PHREEQC-3[55] coupled with Matlab by using the IPhreeqc module.[56] Such coupling allowed combining the capabilities of PHREEQC to model solute transport, as well as kinetic and equilibrium reactions, with the automatic calibration and data analysis capabilities of Matlab.[57−60] The thermodynamic database WATEQ4f, amended with the aqueous speciation reactions of arsenic from Dixit and Hering,[37] was used to calculate the aqueous speciation and reactions. A single set of kinetic model parameters describing the mineral transformation and capable of reproducing the experimental data set under the various

https://doi.org/10.1021/acs.est.2c00309
Environ. Sci. Technol. XXXX, XXX, XXX−XXX

Table 1. Geochemical Reactions and Kinetic Parameters Included in the Reactive Transport Model[a]

Oxidative dissolution of the As-bearing sulfide minerals			
arsenopyrite	$FeAsS + 2.75O_2 + 1.5H_2O \rightarrow Fe^{2+} + H_3AsO_3 + SO_4^{2-}$		
parameter	unit		calibrated value
k_{FeAsS}	$[mol^{-2}\cdot L^3\cdot m^{-2}\cdot s^{-1}]$		2.55×10^{-7} [1.51×10^{-7}; 3.74×10^{-7}]
$x_{1,FeAsS}$	[-]		0.59 [0.51; 0.63]
$x_{2,FeAsS}$	[-]		0.25 [0.22; 0.27]
A_{FeAsS}	$[m^2\cdot mol^{-1}]$		72.65 [53.23; 89.05]
$K_{ox,FeAsS}$	[-]		4.44×10^{-3} [3.18×10^{-3}; 5.67×10^{-3}]
löllingite	$FeAs_2 + 2O_2 + 2H_2O \rightarrow Fe^{2+} + 2H_2AsO_3^-$		
parameter	unit		calibrated value
k_{FeAs2}	$[mol^{-2}\cdot L^3\cdot m^{-2}\cdot s^{-1}]$		1.00×10^{-7} [9.36×10^{-8}; 1.10×10^{-7}]
$x_{1,FeAs_2}$	[-]		0.69 [0.68; 0.69]
$x_{2,FeAs_2}$	[-]		−0.02 [−0.02; −0.01]
A_{FeAs_2}	$[m^2\cdot mol^{-1}]$		140 [134; 144]
$K_{ox,FeAs_2}$	[-]		4.44×10^{-3} [3.18×10^{-3}; 5.67×10^{-3}]
Oxidation of aqueous species			
		k_{Fe_1} $[mol^{-3}\cdot L^4\cdot s^{-1}]$	k_{Fe_2} $[mol^{-1}\cdot L^2\cdot s^{-1}]$
ferric iron	$Fe^{2+} + 0.25O_2 + H^+ \rightarrow Fe^{3+} + 0.5H_2O$	9.84×10^{15}[b]	1.28×10^{-6}[c]
		α [-]	k_{As} $[mol^{-2}\cdot L^3\cdot s^{-1}]$
arsenite	$H_3AsO_3 + 0.5O_2 + H^+ \rightarrow H_2AsO_4^-$	1.05 [0.97; 1.10]	3.74×10^3 [2.56×10^3; 6.81×10^3]
Precipitation of secondary mineral phases			
		$\log(K_{sp})$ [-]	k_m $[mol\cdot s^{-1}]$
ferric arsenate	$Fe^{3+} + 0.5O_2 + AsO_4^{3-} + 2H_2O \rightarrow FeAsO_4\cdot 2H_2O$	27.20 [26.88; 28.57]	1.57×10^{-11} [8.64×10^{-12}; 9.19×10^{-11}]
iron (hydr)oxide	$Fe^{3+} + 2H_2O \rightarrow FeOOH + 3H^+$	−3.68 [−3.88; −3.52]	2.86×10^{-12} [1.73×10^{-12}; 3.50×10^{-12}]

[a]95% confidence intervals of the calibrated parameters are shown in brackets. [b]Haberer et al. (2015).[48] [c]Singer and Stumm (1970).[64]

tested hydrochemical conditions and spatial configurations was calibrated through parallelization of the simulations of columns 1−4. Details regarding the calibration procedure are provided in the Supporting Information. A global sensitivity analysis was performed to assess the relative linear and nonlinear influence of the calibrated model parameters (Table 1) on the model outputs (arsenic elution, mineral dissolution/precipitation, and surface passivation). This sensitivity analysis, presented in the Supporting Information together with the collected experimental data set, shows the importance of constraining the model calibration by observations encompassing a range of hydrochemical, geochemical, and hydrodynamic conditions.[61]

Reaction Network. The model accounts for a series of geochemical processes triggered by the changes in hydrochemistry and by the transition from anoxic to oxic conditions. Such geochemical processes include: (i) the oxidative dissolution of arsenopyrite and löllingite, (ii) the precipitation of iron (hydr)oxides and ferric arsenate phases, (iii) the surface passivation of the As-bearing sulfide minerals induced by the formation of new mineral phases,[7] (iv) the adsorption of arsenic onto freshly precipitated iron (hydr)oxides,[37] and (v) the electrochemical interactions between the quartz sand surface and the aqueous charged species.[62] The abiotic mineral transformations were described with the set of reactions listed in Table 1. These key reactions are controlled by the rate expressions defined by means of thermodynamic constraints and hydrochemical composition.

Dissolution and Precipitation Mechanisms. The dissolution rates of arsenopyrite and löllingite were expressed as a function of (i) oxygen and proton concentrations, (ii) surface areas of the sulfide minerals, and (iii) precipitated iron (hydr)oxide and ferric arsenate phases that coat and passivate the reactive sulfide mineral surfaces[25,31−33,41−43,63]

$$R_m = k_m \times [O_2]^{x_{1,m}} \times [H]^{x_{2,m}} \times (A_m \times \{m\}) \times \frac{1}{1 + \frac{\{FeOOH\} + \{FeAsO_4\}}{\{m\} \times K_{ox,m}}} \quad (1)$$

where k_m is the rate constant, $x_{1,m}$ and $x_{2,m}$ are calibrated exponents, A_m is the exposed surface area of the sulfide mineral $[m^2\cdot mol^{-1}]$, $\{m\}$ is the amount of mineral per unit volume of solution $[mol\cdot L^{-1}]$, and $K_{ox,m}$ is a calibrated constant. Quantities in brackets and braces, [ ] and { }, represent the molar concentration of the dissolved species and minerals, respectively.

The abiotic oxidation of ferrous iron to ferric iron in the presence of oxygen was kinetically controlled by the concentration of the reactants and the pH according to the rate[47,64]

$$R_{Fe} = k_{Fe_1} \times [Fe^{2+}] \times [O_{2(aq)}] \times [OH^-]^2 + k_{Fe_2} \times [Fe^{2+}] \times [O_{2(aq)}] \quad (2)$$

where k_{Fe_1} and k_{Fe_2} are rate constants. The abiotic oxidation of arsenite by oxygen was catalyzed by the oxidation of ferrous iron under circumneutral pH and enhanced under acidic pH[65,66]

$$R_{As} = \alpha \times R_{Fe} + k_{As} \times [As(III)] \times [O_{2(aq)}] \times [H^+] \quad (3)$$

where α is a coefficient coupling the abiotic oxidation rates of ferrous iron and arsenite and k_{As} is a rate constant.

The precipitation of the secondary mineral phases was expressed as a function of the degree of oversaturation of the minerals

$$R_{FeAsO_4} = k_{FeAsO_4\text{-}pptn}(\Omega_{FeAsO_4} - 1)\delta_{\Omega>1} \quad (4)$$

https://doi.org/10.1021/acs.est.2c00309
Environ. Sci. Technol. XXXX, XXX, XXX−XXX

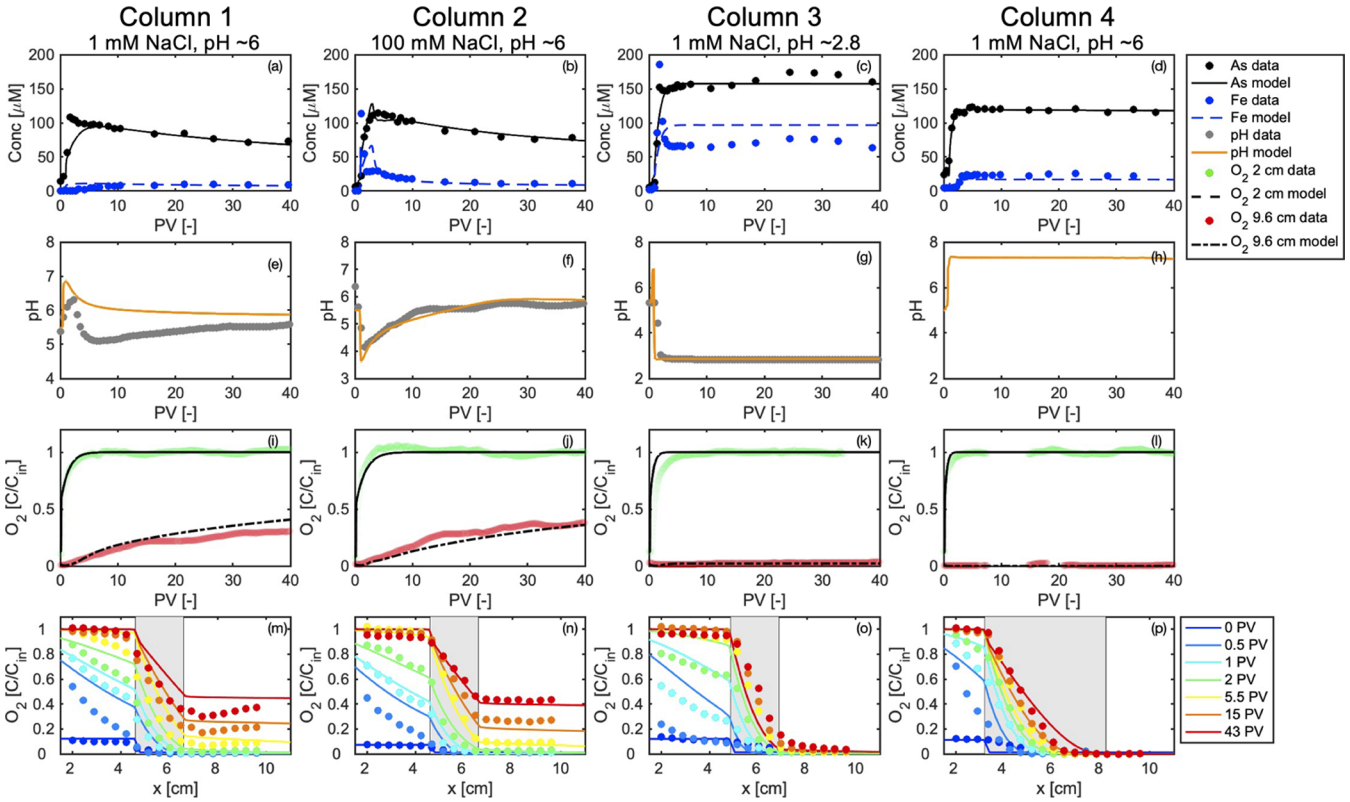

Figure 2. Measured (symbols) and simulated (lines) breakthrough curves of arsenic, iron (a–d), and pH (e–h) at the outlet of the columns (note that pH was not measured in column 4). Oxygen evolution at two locations at a distance of 2 and 9.6 cm from the inlet of the columns (i–l) and oxygen spatial profiles at different times (m–p) during the column experiments 1–4. The gray areas show the location of the reactive As-bearing sulfide mineral inclusions. The hydrochemical compositions of the inlet solutions are specified for each column at the top of the figure.

$$R_{\mathrm{FeOOH}} = k_{\mathrm{FeOOH\text{-}pptn}}(\Omega_{\mathrm{FeOOH}} - 1)\delta_{\Omega>1} \quad (5)$$

where $k_{\mathrm{FeAsO_4}}$ and k_{FeOOH} are the rate constants and Ω_m is the saturation ratio of the mineral m. $\Omega_m = \mathrm{IAP}_m/K_{sp,m}$, where IAP_m and $K_{sp,m}$ are the ion activity product and the solubility product of the mineral m, respectively, with $\delta = 1$ if $\Omega_m > 1$. The total pool of iron (hydr)oxide was represented with a simplified stoichiometry FeOOH in the reactive network.

Surface Complexation. The interactions between protons, major ions, and the quartz sand surface, as well as the adsorption of trace elements onto the freshly precipitated iron (hydr)oxides, were simulated using surface complexation models. The adsorption reactions at the surface of the natural sand are listed in Table S7 and included the protonation and deprotonation of the quartz surface, as well as the formation of Na, Br, and Cl outer-sphere complexes.[62] These reactions were defined for a single type of surface site (i.e., SiOH, 4.6 sites/nm^2) using the *Basic Stern* model with an inner layer capacitance $C_1 = 8.55$ F/m^2. The diffuse double layer (DDL) model of ferrihydrite with a specific surface area of 600 m^2/g and with weak and strong adsorption sites (i.e., $\mathrm{Hfo_w}$ and $\mathrm{Hfo_s}$, respectively)[67] was used to describe the adsorption reactions at the surface of the precipitated iron (details are provided in the Supporting Information). Arsenic adsorption onto the freshly precipitated iron oxides was simulated using the set of surface complexation reactions and parameterization from Dixit and Hering.[37]

Reactive Transport. The transport of oxygen and aqueous charged species in the mobile aqueous phase was described with the governing multicomponent transport equation, accounting for the compound-specific diffusive/dispersive properties, the Coulombic interactions between charged species,[68−70] as well as the kinetic partitioning of oxygen between the aqueous and an entrapped gas phase[42]

$$\theta_w\frac{\partial C_{w,i}}{\partial t} + (1-\theta_w-\theta_g)\rho_s\frac{\partial S_i}{\partial t} + \theta_g\frac{\partial C_{g,i}}{\partial t} + q\frac{\partial C_{w,i}}{\partial x} - \frac{\partial}{\partial x}\left(\sum_{j=1}^{N}\theta_w D_L^{ij}\frac{\partial C_{w,i}}{\partial x}\right) = -\sum_{k=1}^{N_k}\nu_{ik}R_k \quad (6)$$

$$\theta_g\frac{\partial C_{g,O_2}}{\partial t} = \lambda(\mathrm{HC}_{w,O_2} - C_{g,O_2}) \quad (7)$$

where $C_{w,i}$, $C_{g,i}$ [mol·L^{-1}], and S_i [mol·kg^{-1}] are the aqueous, gas phase, and surface concentrations of species i, θ_w and θ_g [-] are the volumetric water and gas content, respectively, q is the specific discharge, ρ_s is the mass density of the solids, and D_L^{ij} is the matrix of longitudinal cross-coupled dispersion coefficients of the charged species in the pore water. R_k [mol·L^{-1}·s^{-1}] and ν_{ik} [-] represent the reaction rate and the corresponding stoichiometric coefficient of species i for the k^{th} reaction and t [s] is the time. λ [s^{-1}] is the kinetic water-gas mass transfer coefficient; H [-] is the Henry's law coefficient. $\lambda = 7.55 \times 10^{-6}$ s^{-1} was determined based on the O_2 transport behavior in a separate conservative flow-through experiment (see the Supporting Information), whereas θ_g was considered as a fitting parameter for each flow-through setup. D_L^{ij} was calculated as[71]

https://doi.org/10.1021/acs.est.2c00309
Environ. Sci. Technol. XXXX, XXX, XXX−XXX

Table 2. Measured Amount of As and Fe Released and O_2 Consumed after 40 PV during the Column Experiments

Experiment	1	2	3	4	5
size inclusion [cm]	2	2	2	4	2
flow velocity [m/day]	1.5	1.5	1.5	1.5	30
ionic strength NaCl [mM]	1	100	1	1	1
injected solution pH	~6	~6	2.8	~6	~6
total arsenic released [μmol]	33.6	35.2	64.5	47.5	5.1
arsenic concentration [μM]	72.9	78.6	160.2	111.3	11.1
total iron released [μmol]	3.2	6.4	28.8	9.1	7.48×10^{-3}
O_2 consumed after 40 PV [%]	81	76	98	99	18

$$D_L^{ij} = \delta_{ij} D_L^i - \frac{z_i z_j D_L^i D_L^j C_{w,i}}{\sum_{k=1}^{N} (z_k^2 D_L^k C_{w,k})} \quad (8)$$

where D_L^i is the longitudinal hydrodynamic dispersion coefficient of species i, δ_{ij} is the Kronecker index which is equal to 1 when $i = j$ and 0 when $i \neq j$, z_i is the charge of species i, and N is the number of mobile species. For each species i, D_L^i was calculated with a linear parameterization[72,73]

$$D_L^i = \theta_w D^i + 0.5 d v \quad (9)$$

where D^i is the aqueous self-diffusion coefficient of specie i calculated and corrected for temperature and viscosity at T = 20 °C (see the Supporting Information), d is the average grain size, and v the flow velocity. The reactive transport model includes a total of 36 species (Table S6) and the 1-D domain representing the column setup was discretized into 50 grid-cells (Δx = 2.3 mm).

RESULTS AND DISCUSSION

Impact of Hydrochemical Conditions. Figure 2 displays the measured and simulated breakthrough curves of arsenic, iron (Figure 2a–d), pH (Figure 2e–h), and oxygen (Figure 2i–l), as well as the spatial profiles of oxygen at different times (Figure 2m–p) in columns 1–4. The results demonstrate the strong impact of the hydrochemical conditions on the dissolution of the As-bearing sulfide minerals and the release of arsenic.

The shift from anoxic to oxic conditions triggers the dissolution of the As-bearing sulfide minerals leading to the release of arsenic and iron which are detected at the outlet of the columns under all tested conditions (Figure 1a–d). Although the concentration of arsenic is of similar magnitude in the four experiments, the dynamics and amounts of arsenic released strongly differ. In column 1, performed under circumneutral and low ionic strength conditions, the arsenic concentration reaches a maximum (108.4 μM) shortly after flushing 1 PV and, then, steadily declines with time. A similar behavior for arsenic is observed in column 2, performed under circumneutral and high ionic strength conditions. However, the maximum concentration (114.5 μM) and the total amount of arsenic released are larger than in column 1. Column 3 was performed by injecting an acidic solution with a low concentration (1 mM) of NaCl as the background electrolyte and the results show a significantly different shape of the arsenic breakthrough curve (Figure 2c). In this case, the arsenic concentration increases sharply at breakthrough time reaching a significantly higher value (i.e., 152.3 μM) than the ones measured in experiments 1 and 2 and remains steady until the end of the experiment. This results in a significantly larger concentration (160.2 μM after 40 PV) and amount of total arsenic released (64.5 μmol after 40 PV) compared to experiments 1 and 2 ([72.9–78.6] μM and [33.6–35.2] μmol after 40 PV). The major species of arsenic is arsenite (average: 90 [84–100]%, 92 [89–98]%, 81 [71–94]% in columns 1, 2, and 3, respectively), although the data show a slight oxidation of arsenite to arsenate upon the introduction of oxygen in the column that is captured by the model (Figure S5).

The breakthrough curves of iron also differ in the three flow-through experiments with the same length of the reactive mineral inclusion (columns 1–3) and can be associated with the behavior of arsenic. In fact, the amount of released arsenic and iron are positively correlated (Table 2). In particular, higher concentration of arsenic in column 2 (high ionic strength), corresponds to the peak of iron detected between 1 and 10 PV (average measured concentration of Fe is 23.6 μM, Figure 2b) in comparison to column 1 (low ionic strength) for which the concentration of Fe remains below 10.2 μM (Figure 2a). In column 3 (acidic conditions), significantly higher and steady concentrations of Fe are observed after 1 PV similar to the As behavior (average concentration of Fe is 71.6 μM, Figure 2c). Furthermore, in both columns 2 and 3, Fe peaks at 1 PV before reaching lower concentration.

Higher concentrations of arsenic and iron are related to lower pH conditions (Figure 2e–g). This is particularly visible in experiment 3, as strong acidic conditions (pH 2.8), prevailing throughout the experiment, prevent the precipitation of iron (hydr)oxide phases. In contrast, the decrease in Fe and As concentrations observed in columns 1 and 2 suggests that the precipitation of secondary mineral phases takes place under the circumneutral pH condition[28] and impacts the dynamics of As concentrations through sequestration mechanisms (i.e., adsorption and coprecipitation) and/or passivation of the sulfide minerals. The effect of pH can also be seen in experiment 2 as a sharp drop in pH, with a minimum value of 3.73 is visible at 1 PV and co-occurs with higher As concentrations. This drop in pH, followed by a sluggish recovery toward the pH value of the injected solution, results from the injection of the NaCl salt solution and the interaction between Na and the surface of the quartz sand, which triggers the deprotonation of the quartz surface.[62] This experimental result illustrates the potential impact that the mineral assemblage (i.e., quartz in this specific case) can exert on the dissolution of As-bearing sulfide mineral by influencing the hydrochemical conditions.

Regarding the propagation of oxygen in the columns, the breakthrough curves and spatial profiles for oxygen are similar in columns 1 and 2 (Figure 2i,j,m-,), while significantly more O_2 is consumed in column 3 (Figure 2k,o). This is in agreement with the arsenic breakthrough curves suggesting similar dissolution of the As-sulfide minerals during the flow-

https://doi.org/10.1021/acs.est.2c00309
Environ. Sci. Technol. XXXX, XXX, XXX−XXX

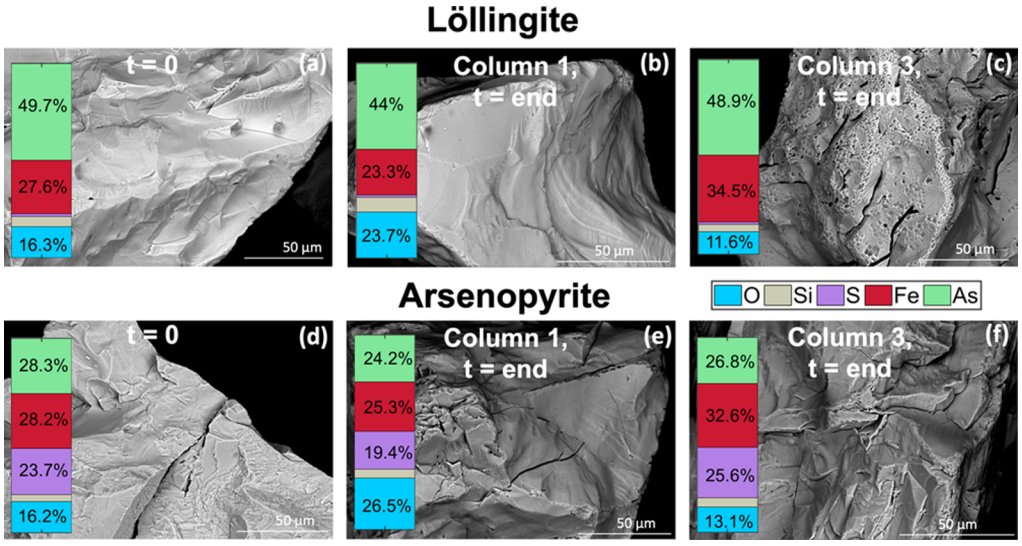

Figure 3. Backscattered electron image of löllingite (a–c) and arsenopyrite (d–f) at the beginning and at the end of the column experiments performed by injecting a circumneutral (column 1) and an acidic solution (column 3). The bar plots summarize the SEM–EDS elemental quantification analyses (in at %) performed on As-bearing sulfide minerals at the beginning and at the end of the column experiments (details of the SEM-EDS analyses are reported in the Supporting Information).

through columns 1 and 2, whereas the acidic conditions in column 3 enhance the dissolution of the As-sulfide minerals and the consumption of oxygen.

The calibrated model could reproduce the complex trends of arsenic, iron, and pH breakthrough curves by explicitly accounting for the impact of the specific hydrochemical conditions (Figure 2). The calibrated model allows us to identify the geochemical mechanisms controlling the dissolution of the sulfide minerals. In particular, we analyze the contribution of mineral phases in releasing and sequestering arsenic, as well as the temporal evolution of the dissolution/precipitation rate and of the passivation of the reactive sulfide mineral surface. The model indicates that although only a minor amount of As-bearing sulfide mineral is consumed during the experiments (<1%), it greatly impacts the hydrochemical conditions and the release of arsenic. The rates of the two minerals are different: löllingite dissolution was significantly faster than that of arsenopyrite (Figure S5), leading to a higher amount of arsenic released from löllingite (i.e., 97, 97, and 77% of the total amount of arsenic released in columns 1, 2, and 3, respectively). This result is corroborated by the low level of sulfur that was measured in all experiments as concentrations remained below the detection limit (6.2 μM) in agreement with the low dissolution of arsenopyrite simulated by the model (see model results for sulfate concentrations in Figure S5). Furthermore, a substantial part of the mobilized arsenic is sequestered in secondary mineral phases in experiments 1 and 2 performed by injecting circumneutral pH solutions (i.e., 40 and 37% in columns 1 and 2, respectively). Arsenic sequestration primarily results from the co-precipitation of arsenic in a ferric arsenate phase, whereas adsorption onto the freshly precipitated iron (hydr)-oxide is minor (<1%). This observation is in agreement with previous findings reporting amorphous ferric arsenate phase precipitation in the presence of high arsenic concentration.[74] Conversely, the strong acidic conditions prevailing in column 3 lower the saturation and prevent the precipitation of the secondary mineral phases. In column 2, the short period of acidic pH conditions induced by the release of protons from the natural sand surface leads to a delay in the precipitation of secondary mineral phases (Figure S5) which explains the higher concentrations of As and Fe at 1 PV compared to column 1.

The experimental and modeling results show that the relative importance of the geochemical mechanisms varies with the tested conditions and that the measured stoichiometric ratio of the aqueous species might not reflect the stoichiometric ratio of the dissolution due to precipitation/sequestration mechanisms. In particular, the global sensitivity analysis, presented in detail in the Supporting Information, indicates that the sensitivities of the model kinetic parameters vary with the hydrogeochemical and hydrodynamic conditions but that all parameters are sensitive across the range of conditions explored in this study.

Effect of pH on the Evolution of Sulfide Mineral Surfaces. The effect of pH on the alteration of sulfide mineral surfaces was investigated by performing SEM and EDS analyses on 186 mineral grains collected at the end of the column experiments 1 and 3, performed under circumneutral and acidic pH conditions, respectively. Figure 3 summarizes the results of these analyses and provides important insights into the fundamental importance of pH in the evolution of the sulfide mineral surface.

Formation of coatings at the surface of the löllingite and arsenopyrite cannot be directly observed from the SEM backscattered electron image. However, SEM–EDS quantification analyses reveal a significant change in the elemental composition of the surface for both sulfide minerals during the column experiments. In particular, under circumneutral pH conditions, the relative proportion of oxygen at the surface of löllingite and arsenopyrite (Figure 3b,e) increases by 45 and 63%, respectively, indicating the formation of freshly precipitated secondary mineral coatings on the surface of the sulfide minerals. The backscattered electron images together with the SEM–EDS quantification analyses suggest that these coatings are thin (<1 μm) and well distributed over the surface of the grains. In contrast, the amount of oxygen in column 3 slightly decreases (29 and 19% for löllingite and arsenopyrite,

https://doi.org/10.1021/acs.est.2c00309
Environ. Sci. Technol. XXXX, XXX, XXX–XXX

respectively), showing that the acidic conditions prevent the formation of coatings. Similar SEM−EDS quantification results were obtained when operating the SEM at 8 keV (Figure S4). Furthermore, backscattered electron images reveal the formation of micrometer-size cavities on the surface of the löllingite grain exposed to acidic conditions (Figure 3c), suggesting higher dissolution of löllingite under acidic conditions.

In order to distinguish the relative contribution of secondary mineral precipitation, surface passivation and the impact of pH on the sulfide mineral dissolution and release of arsenic, additional simulations were performed using the calibrated model in which surface passivation of arsenopyrite and löllingite and/or precipitation of secondary mineral phases were deactivated (Figure 4).

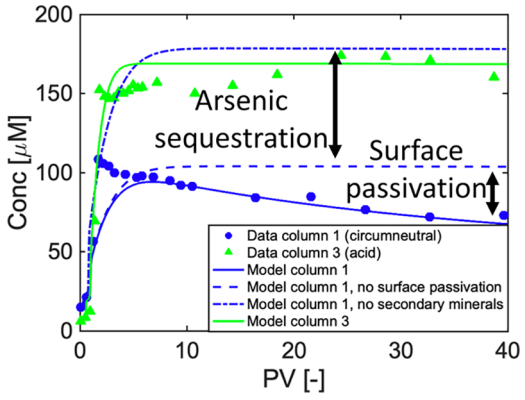

Figure 4. Measured and simulated arsenic breakthrough curves in columns 1 and 3 considering different mechanisms of mineral transformation and arsenic sequestration using the calibrated model.

The simulation results indicate that the direct influence of pH on the reactive minerals dissolution rate (i.e., corrosion) is of minor importance compared to the effect of pH in inhibiting the precipitation of iron (hydr)oxide and ferric arsenate phases. In fact, the precipitation of these secondary minerals is of primary importance since it strongly affects the dissolution of sulfide minerals and the transport of arsenic. Higher acidity prevents surface passivation leading to enhanced dissolution of sulfide minerals as well as significantly lower arsenic sequestration. In particular, the model shows that surface passivation mechanisms hinder the dissolution of sulfide minerals by 26% under the circumneutral conditions prevailing in column 1, whereas sequestration of arsenic into secondary mineral phases leads to a decrease of 70% in As concentration. These results suggest that the cavities visible on the surface of löllingite in Figure 3c result from the absence of surface passivation under acidic conditions which promote the dissolution of the minerals.

Mineral Spatial Distribution Effects. The effects of the spatial distribution of the reactive minerals on the passivation of the As-bearing sulfides through the formation of secondary mineral phases and on the release of arsenic were tested by repeating column 1, initially performed with an inclusion of 2 cm and under low ionic strength conditions, with a longer inclusion of 5 cm (column 4). The comparison of the arsenic breakthrough curves (Figure 2a,d) shows that the amount and dynamics of the arsenic released strongly depend on the size of the inclusion. Interestingly, this difference occurs despite equal concentration of reactants (i.e., bulk mineral and injected oxygen concentrations), similar flow velocity, and an amount of reactive mineral largely in excess compared to the total amount of injected oxygen in both experiments (i.e., <1% of arsenopyrite and löllingite were consumed after 40 PV).

While arsenic concentration peaks at 1 PV and thereafter diminishes due to the passivation of the reactive surface in column 1 (Figure 2a), the maximum As concentration is higher (∼118.1 μM) and remains constant in the experiment performed with a longer inclusion (column 4; Figure 2d). This results in a significantly higher total amount of arsenic released (47.5 μmol after 40 PV in column 4 compared to 33.6 μmol in column 1). Similar to the arsenic breakthrough curve, the iron concentration is higher in column 4 (∼23.1 μM) than in column 1 (<10.7 μM) and remains steady until the end of the experiment. The comparison of the propagation of oxygen between the short and long inclusion cases and the analysis of the measured breakthrough curves confirms that the higher release of As and Fe in column 4 is related to the complete consumption of O_2 within the longer inclusion (Figure 2l). Indeed, O_2 reacts with the sulfide minerals over a longer distance in column 4 and the spatial profiles measured along the column show that almost all oxygen is depleted before 6 cm (Figure 2p). In contrast, in column 1, a significant amount of oxygen is passing through the inclusion and reaches the

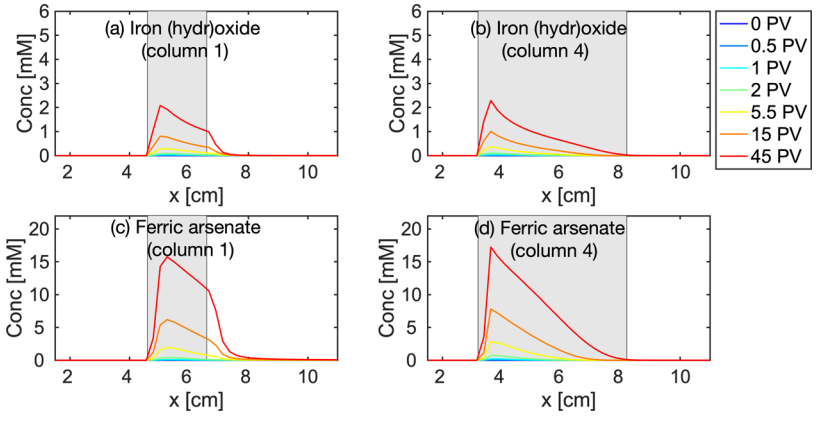

Figure 5. Simulated evolution of the secondary mineral phases in columns 1 and 4 performed by injecting low ionic strength circumneutral solutions. The gray areas show the location of the reactive As-bearing sulfide mineral inclusions. The concentrations of löllingite and arsenopyrite in the inclusions were 2.41 and 2.33 M, respectively.

https://doi.org/10.1021/acs.est.2c00309
Environ. Sci. Technol. XXXX, XXX, XXX−XXX

outlet of the column before the end of the experiment (Figure 2m). The evolution of the reactants and products suggests that the passivation of the mineral reactive surfaces plays a less important role in the system with the longer inclusion. Figure 5 displays the simulated spatial distribution of precipitated secondary mineral phases at different times and shows that the precipitation of such secondary mineral primarily occurs in the upstream portion of the inclusion. This pattern results from the higher concentration of oxygen leading to higher mineral dissolution, dissolved species release, and precipitation rates in the upgradient part of the reactive inclusion (Figure S5). Both oxygen and dissolved iron are progressively depleted along the flow direction, leading to lower precipitation in the downgradient portion of the reactive sulfide mineral inclusion.

The model shows that the spatial extent of secondary mineral precipitation relative to the total length of the inclusion decreases for longer mineral inclusions. Therefore, the effects of surface passivation by the formation of coatings on the overall sulfide mineral dissolution rates occur more rapidly for shorter inclusion. For a longer As-bearing sulfide mineral inclusion, the surface passivation effects on the concentrations of the released aqueous species only become significant at later times, as sufficient coatings hampering oxidative dissolution are progressively distributed over the sulfide minerals surface and as the dissolution front propagates downgradient.

Impact of Hydrodynamic Conditions. We examine the role of flow velocity and time scale of solute transport on the dissolution rate of the sulfide minerals by repeating the first flow-through experiment (column 1, v = 1.5 m/day) with a higher flow velocity (column 5, v = 30 m/day). The breakthrough curves of As and Fe, as well as the propagation of O_2 measured in column 5, indicate that the dissolution of As-bearing sulfide minerals is considerably reduced under high flow velocity (Figure 6).

The maximum As concentration and total amount of arsenic released after 40 PV decreases by nearly 90% under fast flow conditions (14.7 μM) compared to column 1 (108.4 μM). Similar to column 1 (Figure 2a), the concentration of arsenic at the outlet of column 5 decreases after reaching its maximum value at ~5 PV (Figure 6a). This observation suggests that the effect of surface passivation on the dissolution rate of sulfide minerals caused by the precipitation of secondary minerals remains visible under fast transport conditions. Furthermore, less oxygen is consumed by the reactive inclusion and higher O_2 concentrations reach the outlet of the column (Figure 6b).

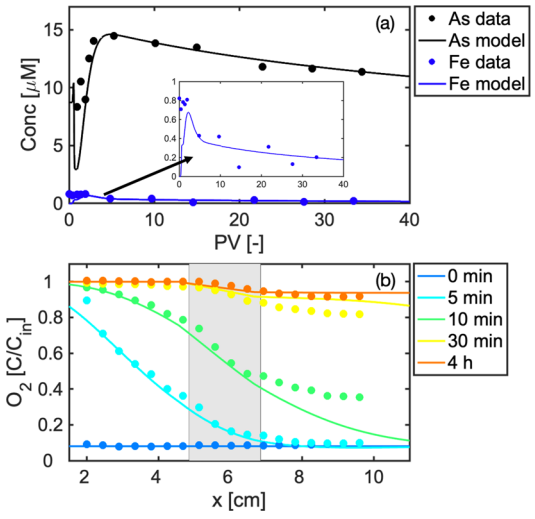

Figure 6. Measured (symbols) and simulated (lines) breakthrough curves of arsenic and iron (a) and oxygen spatial profiles at different times (b) in column experiment 5 that was performed by injecting a 1 mM NaCl, pH ≈ 6 solution with a flow velocity of 30 m/day.

The calibrated model can reproduce the maximum measured arsenic concentration indicating that the overall decrease in the effective rate of sulfide mineral dissolution compared to column 1 is due to the shorter residence time of oxygen (Figure S7). However, in order to capture both the Fe concentration at the outlet and the temporal decrease in As concentration, it was necessary to increase the kinetic mass transfer coefficient of oxygen, the precipitation rates of secondary mineral phases, and the surface passivation factor (eq 1). This may be explained by the enhanced contact between oxygen and the released ferrous iron, which favors the precipitation of secondary mineral phases[75] and the passivation of the sulfide mineral surfaces (Figure S8).

Environmental Significance. The experiments and simulations conducted in this study highlight the complex interactions between multiple co-occurring geochemical mechanisms controlling the dissolution of As-bearing sulfide minerals and the transport of arsenic in groundwater. Such process-based understanding is of pivotal importance for the practical management of groundwater resources both under natural conditions and in the presence of engineered interventions such as managed aquifer recharge, MAR.[20−22] In particular, our results show that the precipitation of secondary mineral phases affects both the dissolution of the sulfide minerals and the mobility of arsenic by promoting the passivation of the sulfide mineral reactive surface and significant sequestration of arsenic. pH plays a key role in the mobilization of arsenic and mineral surface evolution by controlling the dynamics and extent of the secondary mineral phase precipitation. As illustrated in this study by the effects of reactive quartz surfaces on the acidity of the pore water, mineral phases naturally present in the subsurface influence the groundwater hydrochemical conditions and can indirectly but significantly impact the dissolution of sulfide minerals. Furthermore, the mineral spatial distribution and the temporal scale under flow-through conditions are key factors for the kinetics of reactive mineral dissolution and for the mobility of aqueous species in groundwater. In particular, during transient change from anoxic to oxic conditions, the decrease in sulfide mineral reactivity due to surface passivation propagates downgradient. Therefore, the scale of reactive mineral inclusions determines the magnitude and dynamics of surface passivation and its impact on solute concentrations in the subsurface. Our results clearly show that such an effect decreases in the presence of longer inclusions. This finding has important implications for analyzing spatially distributed mineral transformation dynamics and underpins the importance of appropriate scales of investigation to detect and quantify the surface passivation impacts on mineral consumption and reaction product dynamics. Moreover, the relatively high concentrations of arsenic measured in the experiments compared to field measurements (e.g., refs 2 8, and 12) may be representative of the concentrations occurring in the vicinity of dissolving As-bearing sulfide minerals. Such high concentration of arsenic leads to a sequestration mechanism primarily occurring via arsenic-iron co-precipita-

https://doi.org/10.1021/acs.est.2c00309
Environ. Sci. Technol. XXXX, XXX, XXX−XXX

tion into a ferric arsenate phase.[74] In contrast, the adsorption of arsenic onto iron (hydr)oxide is less important under these conditions but is expected to become the dominant mechanism of arsenic sequestration farther away from the sulfide minerals inclusion where ferric arsenate phase precipitation is hampered by the lower arsenic concentration.

Finally, fast flow conditions decrease the overall dissolution rate of sulfide minerals due to shorter solute residence time and consequently lower reaction between O_2 and the reactive minerals. The fast flow conditions also cause an increase in the surface passivation of the sulfide minerals which is interpreted as an enhancement of the reaction between O and the other solutes, in particular Fe(II), leading to higher precipitation of secondary mineral phases and consequently faster coatings of the reactive minerals. Such enhancement could lower the release of arsenic in both natural and engineered systems. However, fast flow conditions could also decrease the adsorption due to incomplete mixing occurring in pore channels at high flow velocity.[76] Mass transfer limitations such as incomplete mixing and intraparticle diffusion[77,78] would, therefore, decrease the arsenic retardation capacity of the porous medium.

The results of this study are of interest for natural fate and transport of geogenic contaminants in groundwater, as well as at the interface between different environmental compartments (e.g., surface/groundwater) where the exchange of atmospheric oxygen and its mixing with anoxic pore water can trigger different biogeochemical reactions.[79−81] The outcomes of this investigation may help designing MAR strategies that minimize the oxidative dissolution of sulfide minerals and the release of arsenic. As an example, infiltration and/or injection rates could be adequately chosen to favor the retention of arsenic in solid phases, thus limiting the risk of freshwater contamination during MAR. Future investigation should also address further geochemical aspects that were not considered in this investigation but will be important in natural settings. For instance, the impact of additional minerals (e.g., carbonates and pyrite) that can control the pore water pH and, thus, the oxidative dissolution of As-bearing minerals. These additional minerals can also affect the hydrochemistry by the release of dissolved species, such as high sulfate concentrations that are often observed in many natural and engineered subsurface systems.[82,83] Finally, the developed process-based model, validated with the experimental observations in the different flow-through experiments, could be extended to multidimensional systems with complex patterns of physical and/or geochemical heterogeneity.[84−91] This will represent a valuable tool to explore arsenic release and reactive mineral dissolution and transformation in different subsurface systems.

■ ASSOCIATED CONTENT

Supporting Information

The Supporting Information is available free of charge at https://pubs.acs.org/doi/10.1021/acs.est.2c00309.

Technical details of the experiments, preparation and characterization of the porous media, correction of the pH breakthrough curves, conservative oxygen transport experiment and modeling, SEM−EDS analyses, calibration procedure and parameter calibration intervals, transport and surface complexation model parameters, simulated temporal change in mineral transformation rates, arsenic speciation data, additional model simulations, and global sensitivity analysis (PDF)

Complete experimental data set for columns 1−5 (XLSX)

■ AUTHOR INFORMATION

Corresponding Author

Massimo Rolle − *Department of Environmental Engineering, Technical University of Denmark, Lyngby 2800, Denmark;* orcid.org/0000-0001-8833-8951; Email: masro@env.dtu.dk

Authors

Lucien Stolze − *Department of Environmental Engineering, Technical University of Denmark, Lyngby 2800, Denmark; Earth and Environmental Sciences Area, Lawrence Berkeley National Laboratory, Berkeley, California 94720, United States*

Maria Battistel − *Department of Environmental Engineering, Technical University of Denmark, Lyngby 2800, Denmark*

Complete contact information is available at: https://pubs.acs.org/10.1021/acs.est.2c00309

Notes

The authors declare no competing financial interest.

■ ACKNOWLEDGMENTS

This study was funded by the Villum Block Fellowship (Villum Fonden, Denmark). M.R. also acknowledges the support of the Independent Research Fund Denmark (GIGA project, grant DFF 7017-00130). We acknowledge the collaboration with PreSens GmbH and the discussion with Dr. Daniela Obermaier and Dr. Robert Meier. We would like to thank the technical assistance of Malgorzata Rizzi, Sinh Nguyen, Mikael Olsson, and Hanne Bøggild (DTU Environment). Constructive comments and suggestions of four anonymous reviewers helped improving the quality of the paper.

■ REFERENCES

(1) Mukherjee, A.; Bhattacharya, P.; Savage, K.; Foster, A.; Bundschuh, J. Distribution of geogenic arsenic in hydrologic systems: Controls and challenges. *J. Contam. Hydrol.* **2008**, *99*, 1−7.

(2) Fendorf, S.; Michael, H. A.; van Geen, A. Spatial and temporal variations of groundwater arsenic in South and Southeast Asia. *Science* **2010**, *328*, 1123−1127.

(3) Schittich, A.-R.; Wünsch, U. J.; Kulkarni, H. V.; Battistel, M.; Bregnhøj, H.; Stedmon, C. A.; McKnight, U. S. Investigating fluorescenet organic-matter composition as a key predictor for arsenic mobility in groundwater aquifers. *Environ. Sci. Technol.* **2018**, *52*, 13027−13036.

(4) Battistel, M.; Jessen, S.; Rolle, M.; Barbieri, M. Model-based interpretation of hydrogeochemistry and arsenic mobility in a low-enthalpy hydrothermal system. J. *J. Geochem. Explor.* **2020**, *214*, 106534.

(5) Podgorski, J.; Berg, M. Global threat of arsenic in groundwater. *Science* **2020**, *368*, 845−850.

(6) Wallis, I.; Prommer, H.; Berg, M.; Siade, A. J.; Sun, J.; Kipfer, R. The river-groundwater interface as a hotspot for arsenic release. *Nat. Geosci.* **2020**, *13*, 288−295.

(7) Thornburg, K.; Sahai, N. Arsenic occurrence, mobility and retardation in sandstone and dolomite formations of the Fox River Valley, Eastern Wisconsin. *Environ. Sci. Technol.* **2004**, *38*, 5087−5094.

(8) Smedley, P. L.; Knudsen, J.; Maiga, D. Arsenic in groundwater from mineralised Proterozoic basement rocks of Burkina Faso. *Appl. Geochim.* **2007**, *22*, 1074−1092.
(9) Peters, S. C. Arsenic in groundwaters in the Northern Appalachian Mountain belt: a review of patterns and processes. *J. Contam. Hydrol.* **2008**, *99*, 8−21.
(10) Kim, K.; Kim, S.-H.; Jeong, G. Y.; Kim, R.-H. Relations of As concentrations among groundwater, soil and bedrock in Chungnam Korea: implications for As mobilization in groundwater according to the As-hosting mineral change. *J. Hazard Mater.* **2012**, *199−200*, 25−35.
(11) Ryan, P. C.; Kim, J. J.; Mango, H.; Hattori, K.; Thompson, A. Arsenic in a fractured slate aquifer system, New England, USA: influence of bedrock geochemistry, groundwater flow paths, redox and ion exchange. *Appl. Geochem.* **2013**, *39*, 181−192.
(12) Bretzler, A.; Stolze, L.; Nikiema, J.; Lalanne, F.; Ghadiri, E.; Brennwald, M. S.; Rolle, M.; Schirmer, M. Hydrogeochemical and multi-tracer investigations of arsenic-effected aquifers in semi-arid West Africa. *Geosci. Front.* **2019**, *10*, 1685−1699.
(13) Bain, J. G.; Blowes, D. W.; Robertson, W. D.; Frind, E. O. Modelling of sulfide oxidation with reactive transport at a mine drainage site. *J. Contam. Hydrol.* **2000**, *41*, 23−47.
(14) Lefebvre, R.; Hockley, D.; Smolensky, J.; Lamontagne, A. Multiphase transfer processes in waste rock piles producing acid mine drainage 2. Applications of numerical simulation. *J. Contam. Hydrol.* **2001**, *52*, 165−186.
(15) Molson, J. W.; Fala, O.; Aubertin, M.; Bussière, B. Numerical simulations of pyrite oxidation and acid mine drainage in unsaturated waste rock piles. *J. Contam. Hydrol.* **2005**, *78*, 343−371.
(16) Brookfield, A. E.; Blowes, D. W.; Mayer, K. U. Integration of field measurements and reactive transport modelling to evaluate contaminant transport at a sulfide mine tailings impoundment. *J. Contam. Hydrol.* **2006**, *88*, 1−22.
(17) Muniruzzaman, M.; Karlsson, T.; Ahmadi, N.; Rolle, M. Multiphase and multicomponent simulation of acid mine drainage in unsaturated mine waste: modeling approach, benchmarks and application examples. *Appl. Geochim.* **2020**, *120*, 104677.
(18) Wallis, I.; Prommer, H.; Simmons, C. T.; Post, V.; Stuyfzand, P. J. Evaluation of conceptual and numerical models for arsenic mobilization and attenuation during managed aquifer recharge. *Environ. Sci. Technol.* **2010**, *44*, 5035−5041.
(19) Lazareva, O.; Druschel, G.; Pichler, T. Understanding arsenic behavior in carbonate aquifers: Implications for aquifer storage and recovery (ASR). *Appl. Geochem.* **2015**, *52*, 57−66.
(20) Prommer, H.; Sun, J.; Helm, L.; Rathi, B.; Siade, A. J.; Morris, R. Deoxygenation prevents arsenic mobilization during deepwell injection into sulfide-bearing aquifers. *Environ. Sci. Technol.* **2018**, *52*, 13801−13810.
(21) Fakhreddine, S.; Prommer, H.; Gorelick, S. M.; Dadakis, J.; Fendorf, S. Controlling arsenic mobilization during managed aquifer recharge: the role of sediment heterogeneity. *Environ. Sci. Technol.* **2020**, *54*, 8728−8738.
(22) Fakhreddine, S.; Prommer, H.; Scanlon, B. R.; Ying, S. C.; Nicot, J.-P. Mobilization of arsenic and other naturally occurring contaminants during managed aquifer recharge: a critical review. *Environ. Sci. Technol.* **2021**, *55*, 2208−2223.
(23) Verplanck, P. L.; Mueller, S. H.; Goldfarb, R. J.; Nordstrom, D. K.; Youcha, E. K. Geochemical controls of elevated arsenic concentration in groundwater, Ester Dome, Fairbanks district, Alaska. *Chem. Geol.* **2008**, *255*, 160−172.
(24) Kreisserman, Y.; Emmanuel, S. Release of particulate iron sulfide during shale-fluid interaction. *Environ. Sci. Technol.* **2018**, *52*, 638−643.
(25) Corkhill, C. L.; Vaughan, D. J. Arsenopyrite oxidation - A review. *Appl. Geochem.* **2009**, *24*, 2342−2361.
(26) Yunmei, Y.; Yongxuan, Z.; Williams-Jones, A. E.; Zhenmin, G.; Dexian, L. A kinetic study of the oxidation of arsenopyrite in acidic solutions: implications for the environment. *Appl. Geochem.* **2004**, *19*, 435−444.
(27) Walker, F. P.; Schreiber, M. E.; Rimstidt, J. D. Kinetics of arsenopyrite oxidative dissolution by oxygen. *Geochim. Cosmochim. Acta* **2006**, *70*, 1668−1676.
(28) Yu, Y.; Zhu, Y.; Gao, Z.; Gammons, C. H.; Li, D. Rates of Arsenopyrite Oxidation by Oxygen and Fe(III) at pH 1.8−12.6 and 15−45 °C. *Environ. Sci. Technol.* **2007**, *41*, 6460−6464.
(29) McKibben, M. A.; Tallant, B. A.; del Angel, J. K. Kinetics of inorganic arsenopyrite oxidation in acidic aqueous solutions. *Appl. Geochem.* **2008**, *23*, 121−135.
(30) Jakus, N.; Mellage, A.; Höschen, C.; Maisch, M.; Byrne, J. M.; Mueller, C. W.; Grathwohl, P.; Kappler, A. Anaerobic neutrophilic pyrite oxidation by a chemolithoautotrophic nitrate-reducing iron(II)-oxidizing culture enriched from a fractured aquifer. *Environ. Sci. Technol.* **2021**, *55*, 9876−9884.
(31) Lengke, M. F.; Sanpawanitchakit, C.; Tempel, R. N. The oxidation and dissolution of arsenic-bearing sulfides. *Can. Mineral.* **2009**, *47*, 593−613.
(32) Asta, M. P.; Cama, J.; Ayora, C.; Acero, P.; de Giudici, G. Arsenopyrite dissolution rates in O_2-bearing solutions. *Chem. Geol.* **2010**, *273*, 272−285.
(33) Asta, M. P.; Pérez-López, R.; Román-Ross, G.; Illera, V.; Cama, J.; Cotte, M.; Tucoulou, R. Analysis of the iron coatings formed during marcasite and arsenopyrite oxidation at neutral-alkaline conditions. *Geol. Acta* **2013**, *11*, 465−481.
(34) Hansel, C. M.; Benner, S. G.; Fendorf, S. Competing Fe(II)-induced mineralization pathways of ferrihydrite. *Environ. Sci. Technol.* **2005**, *39*, 7147−7153.
(35) Stachowicz, M.; Hiemstra, T.; van Riemsdijk, W. H. Surface speciation of As(III) and As(V) in relation to charge distribution. *J. Colloid Interface Sci.* **2006**, *302*, 62−75.
(36) Xu, T.; Catalano, J. Effects of ionic strength on arsenate adsorption at aluminium hydroxide-water interfaces. *Soils* **2018**, *2*, 1−13.
(37) Dixit, S.; Hering, J. G. Comparison of arsenic(V) and arsenic(III) sorption onto iron oxide minerals: implications for arsenic mobility. *Environ. Sci. Technol.* **2003**, *37*, 4182−4189.
(38) Harvey, M. C.; Schreiber, M. E.; Rimstidt, J. D.; Griffith, M. M. Scorodite dissolution kinetics: implications for arsenic release. *Environ. Sci. Technol.* **2006**, *40*, 6709−6714.
(39) Schwertmann, U.; Cornell, R. M. *Iron Oxides in the Laboratory—Preparation and Characterization*; Wiley-VCH: Weinheim, 2000.
(40) Li, L.; Steefel, C. I.; Yang, L. Scale dependence of mineral dissolution rates within single pores and fractures. *Geochim. Cosmochim. Acta* **2008**, *72*, 360−377.
(41) Salehikhoo, F.; Li, L.; Brantley, S. L. Magnesite dissolution rates at different spatial scales: the role of mineral spatial distribution and flow velocity. *Geochim. Cosmochim. Acta* **2013**, *108*, 91−106.
(42) Fakhreddine, S.; Lee, J.; Kitanidis, P. K.; Fendorf, S.; Rolle, M. Imaging geochemical heterogeneities using inverse reactive transport modeling: an example relevant for characterizing arsenic mobilization and distribution. *Adv. Water Res.* **2016**, *88*, 186−197.
(43) Battistel, M.; Muniruzzaman, M.; Onses, F.; Lee, J.; Rolle, M. Reactive fronts in chemically heterogeneous porous media: experimental and modeling investigation of pyrite oxidation. *Appl. Geochem.* **2019**, *100*, 77−89.
(44) Battistel, M.; Stolze, L.; Muniruzzaman, M.; Rolle, M. Arsenic release and transport during oxidative dissolution of spatially-distributed sulfide minerals. *J. Hazard Mater.* **2021**, *409*, 124651.
(45) Steefel, C. I.; Appelo, C. A. J.; Arora, B.; Jacques, D.; Kalbacher, T.; Kolditz, O.; Lagneau, V.; Lichtner, P. C.; Mayer, K. U.; Meeussen, J. C. L.; Molins, S.; Moulton, D.; Shao, H.; Šimůnek, J.; Spycher, N.; Yabusaki, S. B.; Yeh, G. T. Reactive transport codes for subsurface environmental simulation. *Comput. Geosci.* **2015**, *19*, 445−478.
(46) Stolze, L.; Zhang, D.; Guo, H.; Rolle, M. Model-based interpretation of groundwater arsenic mobility during in situ reductive transformation of ferrihydrite. *Environ. Sci. Technol.* **2019**, *53*, 6845−6854.

https://doi.org/10.1021/acs.est.2c00309
Environ. Sci. Technol. XXXX, XXX, XXX−XXX

(47) Muniruzzaman, M.; Karlsson, T.; Ahmadi, N.; Kauppila, P. M.; Kauppila, T.; Rolle, M. Weathering of unsaturated waste rocks from Kevitsa and Hitura mines: Pilot-scale lysimeter experiments and reactive transport modeling. *Chem. Geol.* **2021**, *130*, 104984.
(48) Haberer, C. M.; Muniruzzaman, M.; Grathwohl, P.; Rolle, M. Diffusive-dispersive fronts in porous media: iron(II) oxidation at the unsaturated-saturated interface. *Vadose Zone J.* **2015**, *14*, 1−14.
(49) Jessen, S.; Postma, D.; Larsen, F.; Nhan, P. Q.; Hoa, L. Q.; Trang, P. T. K.; Long, T. V.; Viet, P. H.; Jakobsen, R. Surface complexation modeling of groundwater arsenic mobility: Results of a forced gradient experiment in a Red River flood plain aquifer, Vietnam. *Geochim. Cosmochim. Acta* **2012**, *98*, 186−201.
(50) Meng, X.; Wang, W. Speciation of Arsenic by Disposal Cartridges. *Proceedings of the 3rd International Conference on Arsenic Exposure and Health Effects. Society for Environmental Geochemistry and Health*; University of Colorado: Denver, 1998.
(51) Manning, A. H.; Solomon, D. K. An integrated environmental tracer approach to characterizing groundwater circulation in a mountain block. *Water Resour. Res.* **2005**, *41*, W12412.
(52) Magal, E.; Weisbrod, N.; Yakirevich, A.; Kurtzman, D.; Yechieli, Y. Line-source multi-tracer test for assessing high groundwater velocity. *Groundwater* **2010**, *48*, 892−897.
(53) Kahler, D. M.; Kabala, Z. J. Acceleration of groundwater remediation by deep sweeps and vortex injections induced by rapidly pulsed pumping. *Water Resour. Res.* **2016**, *52*, 3930−3940.
(54) Gerenday, S. P.; Clark, J. F.; Hansen, J.; Fischer, I.; Koreny, J. Sulfur hexafluoride and potassium bromide as groundwater tracers for managed aquifer recharge. *Groundwater* **2020**, *58*, 777−787.
(55) Parkhurst, D.; Appelo, C. Description of Input and Examples for PHREEQC Version 3—A Computer Program for Speciation, Batch-Reaction, One-Dimensional Transport, and Inverse Geochemical Calculations. 2013, In U. G. Methods, book 6, chap. A43,497 p., available only at http://pubs.usgs.gov/tm/06/a43.
(56) Charlton, S. R.; Parkhurst, D. L. Modules based on the geochemical model PHREEQC for use in scripting and programming languages. *Comput. Geosci.* **2011**, *37*, 1653−1663.
(57) Muniruzzaman, M.; Rolle, M. Modeling multicomponent ionic transport in groundwater with IPhreeqc coupling: Electrostatic interactions and geochemical reactions in homogeneous and heterogeneous domains. *Adv. Water Resour.* **2016**, *98*, 1−15.
(58) Stolze, L.; Zhang, D.; Guo, H.; Rolle, M. Surface complexation modeling of arsenic mobilization from goethite: Interpretation of an in-situ experiment. *Geochim. Cosmochim. Acta* **2019**, *248*, 274−288.
(59) Sprocati, R.; Masi, M.; Muniruzzaman, M.; Rolle, M. Modeling electrokinetic transport and biogeochemical reactions in porous media: a multidimensional Nernst-Planck-Poisson approach with PHREEQC coupling. *Adv. Water Res.* **2019**, *127*, 134−147.
(60) Sprocati, R.; Gallo, A.; Sethi, R.; Rolle, M. Electrokinetic delivery of reactants: pore water chemistry controls transport, mixing and degradation. *Environ. Sci. Technol.* **2021**, *55*, 719−729.
(61) Siade, A. J.; Bostick, B. C.; Cirpka, O. A.; Prommer, H. Unraveling biogeochemical complexity through better integration of experiments and modeling. *Environ. Sci.: Processes Impacts* **2021**, *23*, 1825−1833.
(62) Stolze, L.; Wagner, J. B.; Damsgaard, C. D.; Rolle, M. Impact of surface complexation and eletrostatic interactions on pH front propagation in silica porous media. *Geochim. Cosmochim. Acta* **2020**, *277*, 132−149.
(63) Williamson, M. A.; Rimstidt, J. D. The kinetics and electrochemical rate-determining step of aqueous pyrite oxidation. *Geochim. Cosmochim. Acta* **1994**, *58*, 5443−5454.
(64) Singer, P. C.; Stumm, W. Acidic Mine Drainage: the rate-determining step. *Science* **1970**, *167*, 1121−1123.
(65) Hug, S. J.; Leupin, O. Iron-catalyzed oxidation of arsenic(III) by oxygen and by hydrogen peroxide: pH-dependent formation of oxidants in the Fenton reaction. *Environ. Sci. Technol.* **2003**, *37*, 2734−2742.
(66) Wang, Z.; Fu, Y.; Wang, L. Abiotic oxidation of arsenite in natural and engineered systems: mechanisms and related controversies over the last two decades (1999-2020). *J. Hazard Mater.* **2021**, *414*, 125488.
(67) Dzombak, D. A.; Morel, F. M. M. F. *Surface Complexation Modeling: Hydrous Ferric Oxide*; Wiley, 1990.
(68) Appelo, C. A. J.; Wersin, P. Multicomponent diffusion modeling in clay systems with application to the diffusion of tritium, iodide, and sodium in opalinus clay. *Environ. Sci. Technol.* **2007**, *41*, 5002−5007.
(69) Muniruzzaman, M.; Haberer, C. M.; Grathwohl, P.; Rolle, M. Multicomponent ionic dispersion during transport of electrolytes in heterogeneous porous media: Experiments and model-based interpretation. *Geochim. Cosmochim. Acta* **2014**, *141*, 656−669.
(70) Rolle, M.; Chiogna, G.; Hochstetler, D. L.; Kitanidis, P. K. On the importance of diffusion and compound-specific mixing for groundwater transport: an investigation from pore to field scale. *J. Contam. Hydrol.* **2013**, *153*, 51−68.
(71) Muniruzzaman, M.; Rolle, M. Experimental investigation of the impact of compound-specific dispersion and electrostatic interactions on transient transport and solute breakthrough. *Water Resour. Res.* **2017**, *53*, 1189−1209.
(72) Guedes de Carvalho, J. R. F.; Delgado, J. M. P. Q. Overall map and correlation of dispersion data for flow through granular packed beds. *Chem. Eng. Sci.* **2005**, *60*, 365−375.
(73) Kurotori, T.; Zahasky, C.; Hosseinzadeh Hejazi, S. A.; Shah, S. M.; Benson, S. M.; Pini, R. Measuring, imaging and modelling solute transport in a microporous limestone. *Chem. Eng. Sci.* **2019**, *196*, 366−383.
(74) Drahota, P.; Filippi, M. Secondary arsenic minerals in the environment: a review. *Environ. Inter.* **2009**, *35*, 1243−1255.
(75) Edwards, B. A.; Ferris, F. G. Influence of water flow on in situ rates of bacterial Fe(II) oxidation. *Geomicrobiol. J.* **2020**, *37*, 67−75.
(76) Stolze, L.; Rolle, M. Surface complexation reactions in sandy porous media: effects of incomplete mixing and mass-transfer limitations in flow-through systems. *J. Contam. Hydrol.* **2022**, *246*, 103965.
(77) Fesch, C.; Simon, W.; Haderlein, S. B.; Reichert, P.; Schwarzenbach, R. P. Nonlinear sorption and nonequilibrium solute transport in aggregated porous media: experiments, process identification and modeling. *J. Contam. Hydrol.* **1998**, *31*, 373−407.
(78) Grathwohl, P. *Diffusion in Natural Porous Media: Contaminant Transport, Sorption/Desorption and Dissolution Kinetics*; Kluwer Academic Publishers: Boston, MA, 1998.
(79) Datta, S.; Mailloux, B.; Jung, H.-B.; Hoque, M. A.; Stute, M.; Ahmed, K. M.; Zheng, Y. Redox trapping of arsenic during groundwater discharge in sediments from the Meghna riverbank in Bangladesh. *PNAS* **2009**, *106*, 16930−16935.
(80) Rolle, M.; Le Borgne, T. Mixing and reactive fronts in the subsurface. *Rev. Mineral. Geochem.* **2019**, *85*, 111−142.
(81) Ahmadi, N.; Heck, K.; Rolle, M.; Helmig, R.; Mosthaf, K. On multicomponent gas diffusion and coupling concepts for porous media and free flow: a benchmark study. *Comput. Geosci.* **2021**, *25*, 1493−1507.
(82) Salmon, S. U.; Rate, A. W.; Rengel, Z.; Appleyard, S.; Prommer, H.; Hinz, C. Reactive transport controls on sandy acid sulfate soils and impacts on shallow groundwater quality. *Water Resour. Res.* **2014**, *50*, 4924−4952.
(83) Lindsay, M. B. J.; Moncur, M. C.; Bain, J. G.; Jambor, J. L.; Ptacek, C. J.; Blowes, D. W. Geochemical and mineralogical aspects of sulfide mine tailings. *Appl. Geochem.* **2015**, *57*, 157−177.
(84) Li, L.; Gawande, N.; Kowalsky, M. B.; Steefel, C. I.; Hubbard, S. S. Physicochemical heterogeneity controls on uranium bioreduction rates at the field scale. *Environ. Sci. Technol.* **2011**, *45*, 9959−9966.
(85) Chiogna, G.; Rolle, M.; Bellin, A.; Cirpka, O. A. Helicity and flow topology in three-dimensional anisotropic porous media. *Adv. Water Resour.* **2014**, *73*, 134−143.
(86) Ye, Y.; Chiogna, G.; Cirpka, O.; Grathwohl, P.; Rolle, M. Enhancement of plume dilution in two-dimensional and three-dimensional porous media by flow focusing in high-permeability inclusions. *Water Resour. Res.* **2015**, *51*, 5582−5602.

https://doi.org/10.1021/acs.est.2c00309
Environ. Sci. Technol. XXXX, XXX, XXX−XXX

(87) Jung, H.; Navarre-Sitchler, A. Scale effect on the time dependence of mineral dissolution rates in physically heterogeneous porous media. *Geochim. Cosmochim. Acta* **2018**, *234*, 70−83.
(88) Wang, L.; Wen, H.; Li, L. Scale dependence of surface complexation capacity and rates in heterogeneous media. *Sci. Total Environ.* **2018**, *635*, 1547−1555.
(89) Muniruzzaman, M.; Rolle, M. Multicomponent ionic transport modeling in physically and electrostatically heterogeneous porous media with phreeqcRM coupling for geochemical reactions. *Water. Res.* **2019**, *55*, 11121−11143.
(90) Muniruzzaman, M.; Rolle, M. Impact of diffuse layer processes on contaminant forward and back diffusion in heterogeneous sandy-clayey domains. *J. Contam. Hydrol.* **2021**, *237*, 103754.
(91) Cogorno, J.; Stolze, L.; Muniruzzaman, M.; Rolle, M. Dimensionality effects on multicomponent ionic transport and surface complexation in porous media. *Geochim. Cosmochim. Acta* **2022**, *318*, 230−246.

https://doi.org/10.1021/acs.est.2c00309
Environ. Sci. Technol. XXXX, XXX, XXX−XXX